Article:
Owen, L.R., Jones, N.G., Stone, H.J. et al. (2024) Separation of static and dynamic displacements in the CrMnFeCoNi high entropy alloy. Acta Materialia, 262. 119164. ISSN: 1359-6454

https://doi.org/10.1016/j.actamat.2023.119164

Separation of static and dynamic displacements in the CrMnFeCoNi high entropy alloy

L.R. Owen[a,*], N.G. Jones[b], H.J. Stone[b], H.Y. Playford[c]

[a]*Department of Materials Science and Engineering, University of Sheffield, S1 3JD, UK*
[b]*Department of Materials Science and Metallurgy, University of Cambridge, CB3 0FS, UK*
[c]*ISIS Facility, STFC Rutherford Appleton Laboratory, Didcot, Oxfordshire, OX11 0QX, UK*

Abstract

Assessing the local lattice strains in high-entropy alloys (HEAs) is essential if their mechanical properties are to be rationalised and the validity of the highly distorted lattice hypothesis is to be determined. To accomplish this, direct measurements of local distortions need to be made, and the thermal component separated. In this study, variable temperature neutron total scattering measurements were made on the exemplar HEA CrMnFeCoNi, along with pure nickel and an alloy of Ni-37.5Co25Cr25at.%. A number of methods of determining local atomic displacements from such measurements were used and their efficacy for determining local lattice strains discussed. Using these methods, the local lattice strains have been effectively quantified. The data suggest the HEA does have a comparatively higher strain than the NiCoCr alloy, however, the alloying strains are small in comparison to the thermal component in all cases. As such, whether the local lattice strains are significant and can class the alloy as highly strained remains inconclusive.

Keywords: *`High entropy alloys, Local lattice strains, Total Scattering, Pair Distribution Function`

1. Introduction

High entropy alloys remain one of the most active fields in international metallurgical research and recent developments have been the subject of extensive reviews [1, 2, 3, 4, 5]. Of the four principles put forward to explain the properties of High Entropy alloys (HEA) [6], the highly-distorted lattice hypothesis remains one of the least investigated. It has been suggested [7] that the random occupation of atomic sites in a crystalline material by elements of different

*Corresponding author
Email address: `lewis.owen@sheffield.ac.uk` (L.R. Owen)

size necessarily results in a high level of local distortion [1]. Such distortions are known to strongly effect the observed physical properties of single phase solid solutions, such as increased hardness and reduced electrical and thermal conductivity [8]. However, the amount of distortion that is actually present within these structures remains poorly understood. In particular, it remains unclear whether these materials are significantly more distorted than compositionally simpler lower order solid solutions (e.g. binary and ternary alloys). At present, direct analysis of the level of distortion is still sparse within the literature, as noted in previous reviews on the topic [9, 10]. This may be attributed to the lack of suitable techniques for probing such information, or the presence of complicating factors in the assessment of the data.

In previous work we reported an assessment of the local lattice strain in the exemplar HEA CrMnFeCoNi and compared the results to several compositionally simpler systems [11]. These analyses were carried out using the total scattering method, comparing pair distribution functions (PDFs) measured at room temperature. It was noted that the PDF peak width is a function of both the static displacements (local-lattice strains) and dynamic displacements (thermal oscillations). Consequently, to provide an accurate assessment of the magnitude of the static displacements in isolation, it is necessary to separate the thermal contribution from the offsite displacement. It should be noted that local lattice strains refer to static displacements away from their idealised site [2], due to atomic size differences within the material and are distinct from other types of lattice strain often more traditionally analysed in engineering materials (for example macroscopic Type I strains, microstructural Type II strains, or Type III strains related to dislocations with a material). A more complete discussion of this can be found in [9], [10] and [13].

Several methods have been proposed for the direct measurement of local lattice strains. These include from total scattering or PDF measurements [11, 14], EXAFS [15, 16], HR-TEM [17] and *ab initio* DFT calculations [15, 18, 19]. The relative merits of these methods for the assessment of local lattice strains in high entropy alloys have recently been reviewed in [10]. As the measured offsite displacements are susceptible to both static and dynamic contributions, variable temperature studies are required to either determine the functional variation with temperature or eliminate the thermal contribution completely by measurement under cryogenic conditions.

Some previous attempts have been made to isolate the static component from the thermal, by reducing the temperature. Okamoto et al. [20] attempted to isolate the thermal component by reducing the temperature to 25K, measuring the local atomic displacement from a series of single crystal samples using

[1] It is noted that in strict crystallographic terms, the lattice itself cannot be distorted; however the community uses the term lattice synonymously with crystal structure, and so the same shall be done here.

[2] The definition of a strain requires both a change in length and a reference length, normally in this case taken to be the atomic radius; however, other references are possible and the reader is referred to [12] for discussion on this point

synchrotron X-ray diffraction (XRD). In their analysis they assumed that the local displacement would solely arise from the static component at this temperature. However, it is unclear whether this temperature was sufficient to fully eliminate the thermal contributions to the lattice displacements. More recently, Tan et al. [21] performed a variable temperature study using synchrotron XRD down to 5K. The variation in peak intensity as a function of angle was used to measure the Debye-Waller factor; however, they were unable to isolate the static component. The suitability of using Debye-Waller factors from Rietveld fitting of Bragg peaks to provide a measure of the offsite displacements, as opposed to direct measurements from the PDF, will be discussed in this paper.

In this work, a method is described for the separation of static and dynamic displacements using total scattering data and PDFs measured at different temperatures. By recording the level of offsite displacement at temperatures towards absolute zero, the variation in thermal displacement as a function of temperature may be isolated. The level of instrumental broadening of the data may also be determined through the use of a comparative pure element standard. From knowledge of these two effects, it is shown that it is possible to isolate the static offsite component of the material, and hence provide a quantitative measure of the local lattice distortion of the crystal structure. To demonstrate the efficacy of this approach, in this study the ternary system NiCoCr and classic HEA CrMnFeCoNi are studied, along with a pure nickel standard, to elucidate the level of static strain in these important systems.

2. Background theory

2.1. Thermal oscillations

At a finite temperature it is assumed that atoms in a crystalline material have sufficient thermal energy to undergo oscillations away from their idealised atomic positions. It is well established that the effect of thermal oscillations on the Bragg diffraction data can be modelled by the introduction of a thermal decay parameter, the Debye-Waller factor (B) [22, 23]. This may be accounted for by the incorporation of a thermally decaying atomic scattering factor as follows:

$$f = f_0 \exp\Big(- \frac{B \sin^2 \theta}{\lambda^2} \Big) \tag{1}$$

where B is the Debye-Waller factor, θ the scattering angle, f_0 the atomic scattering factor and λ the wavelength. It is often useful to relate the Debye-Waller factor (B) to the isotropic displacement parameter U_{iso} by:

$$B = 8\pi^2 U_{\mathrm{iso}} \tag{2}$$

The U_{iso} is, in turn, related to the offsite displacements (u) as:

$$U_{\mathrm{iso}} = < u^2 > \tag{3}$$

Alternatively, the root mean squared atomic displacement may be quoted as $u_{\mathrm{rms}} = \sqrt{U_{\mathrm{iso}}} = \sqrt{< u^2 >}$

Owing to the high symmetry (cubic) nature of the alloys chosen in this study, it is reasonable to assume that the oscillations in the three crystallographic directions will be the same. For lower symmetry materials, it is possible for the magnitudes of the oscillations to vary with direction, however, this will not be considered in the following analysis.

2.2. Debye-Waller factor relationship to temperature

The Debye-Waller factor is temperature dependent and, for *fcc* metals in the harmonic first nearest neighbour approximation, obeys the following equation [24]:

$$B = \frac{24\pi^2\hbar^2}{Mk{\theta_D}^2}T\Big(f(x) + \frac{x}{4}\Big) \tag{4}$$

where:

$$x = \frac{\theta_D}{T} \tag{5}$$

and:

$$f(x) = \frac{1}{x}\int_0^x \frac{y}{\exp y - 1}dy \tag{6}$$

in which $\hbar$ is the Planck constant, M the atomic mass, k is the Boltzmann constant, T the absolute temperature, and θ_D the Debye temperature. It should be noted that when $T > \theta_D$, it follows that $x < 1$ and

$$f(x) + \frac{x}{4} \approx 1 \tag{7}$$

and hence:

$$B = \frac{24\pi^2\hbar^2}{Mk{\theta_D}^2}T \tag{8}$$

Therefore, for temperatures above the Debye temperature the change in the Debye-Waller factor with temperature is approximately linear. Conversely, at low temperature, i.e. as $T \to 0$, then $x \to \infty$, $f(x) \to 0$ and hence:

$$B \to \frac{6\pi^2\hbar^2}{Mk\theta_D} \tag{9}$$

i.e. the Debye-Waller factor tends to a constant that is dependent on the mass of the oscillating atoms and the Debye temperature of the material.

2.3. Static and dynamic displacements

The substitution of an atom in a structure by one of a different atomic radius will result in an offsite static displacement of the surrounding atoms away from their idealised atomic positions. These displacements would be expected to be isotropic away from the substituent. Additionally, the atoms will experience thermal oscillations around their new atomic positions. In the time averaged conditions of a diffraction experiment the contributions from the static displacement and the thermal oscillations will therefore be convolved with one another.

Assuming that the offsite displacements away from idealised atomic sites, caused by the static distortion, are described by a normal distribution with mean $\mu_{u,S} = 0$ and standard deviation $\sigma_{u,S}$, the distribution may be described as:

$$n_S(u) = \frac{1}{\sigma_{u,S}\sqrt{2\pi}} \exp\Big(- \frac{u^2}{2\sigma_{u,S}^2}\Big) \tag{10}$$

Similarly, the dynamic thermal displacements can be described by a normal distribution with mean $\mu_{u,T} = 0$ and standard deviation $\sigma_{u,T}$:

$$n_T(u) = \frac{1}{\sigma_{u,T}\sqrt{2\pi}} \exp\Big(- \frac{u^2}{2\sigma_{u,T}^2}\Big) \tag{11}$$

Therefore, the resultant distribution:

$$n = n_S(u) * n_T(u) = \frac{1}{\sigma_u\sqrt{2\pi}} \exp\Big(- \frac{u^2}{2\sigma_u^2}\Big) \tag{12}$$

where:

$$\sigma_u^2 = \sigma_{u,S}^2 + \sigma_{u,T}^2 \tag{13}$$

It should be noted that for a Gaussian distribution the root mean squared displacement away from the mean is equal to the standard deviation of the distribution, $U_S =< u_s^2 >= \sigma_S^2$. Therefore, eq. 13 can be rewritten as:

$$U_u = U_S + U_T \tag{14}$$

where U_S and U_T are the atomic displacement parameters caused by the static and dynamic (thermal) displacements respectively.

A similar consideration can then be made of the interatomic distances, l. Consider two atoms, one at the origin and the second displaced by a distance μ_l. The distribution of atoms around the origin can be described using the distribution from eq. 12:

$$n_A(l) = \frac{1}{\sigma_u\sqrt{2\pi}} \exp\Big(- \frac{l^2}{2\sigma_u^2}\Big) \tag{15}$$

Similarly for the atoms at a distance μ_l:

$$n_B(l) = \frac{1}{\sigma_u\sqrt{2\pi}} \exp\Big(- \frac{(l-\mu_l)^2}{2\sigma_u^2}\Big) \tag{16}$$

Therefore the distribution of interatomic distances, n_{AB}, is given as:

$$n_{AB}(l) = n_A(l) \times n_B(l) = \frac{1}{\sigma_l\sqrt{2\pi}} \exp\Big(- \frac{(l-\mu_l)^2}{2\sigma_l^2}\Big) \tag{17}$$

where:

$$\sigma_l^2 = \sigma_u^2 + \sigma_u^2 = 2\sigma_u^2 \tag{18}$$

$$\sigma_l = \sqrt{2}\sigma_u \tag{19}$$

and noting the relationship in equation 13.

These relationships will allow the interconversion between the various measured physical properties that will be discussed. As described in [12] from these values, two numerical quantifiers of local lattice strain can be used as:

$$\varepsilon_{u,S} = \frac{\sigma_{u,S}}{\bar{r}} \quad \text{and} \quad \varepsilon_{l,S} = \frac{\sigma_{l,S}}{\mu_l} \tag{20}$$

where $\varepsilon_{u,S}$ is the local strain in terms of the offsite displacement, $\bar{r}$ the average atomic radius, and $\varepsilon_{l,S}$ is the local strain in terms of the variation in bond length. The different measures are dependent on the property that is capable of being captured by the measurement technique.

3. Experimental method

3.1. Materials

The experiment methodology for this work follows that described in [11]. Powders of Ni-37.5Co-25at.%Cr and equiatomic CrMnFeCoNi were prepared by gas atomisation by Hauner Metallische Werkstoffe. A sample of pure Ni powder was obtained commercially, and with the two previous samples formed the set of samples investigated. A small quantity of each powder sample was sealed in a quartz tube, following evacuation and back-filling with Ar, prior to heat treatment at 1200°C for 2 h and subsequent quenching in ice water. The heat treatment served to chemically homogenise the samples, sinter them into a formable solid, as well as reducing any microstrains in the material that may have arisen during the atomisation process. Samples were subsequently turned down to a cylindrical geometry with diameter $\sim$ 6 mm, and height $\geq$40mm.

3.2. Neutron scattering

Neutron total scattering data were collected from the three samples (referred to as Ni, NiCoCr and CrMnFeCoNi) on the Polaris diffractometer at the ISIS Pulsed Neutron and Muon Source, at temperatures from 4K to 291K. The temperatures at which the samples were measured and the corresponding homologous temperatures ($T_H = T/T_m$) can be found in Table 1. Samples were initially measured at room temperature, before cooling to 4K, and then at gradually increasing temperatures. Measurements were carried out for 2 h at each temperature point. Temperatures were chosen such that the samples were measured at the same homologous temperatures.

3.3. Data Analysis

The data were processed using the Mantid software [25, 26] to focus, correct, and normalise the signals from the individual detector elements and yield powder diffraction patterns. Rietveld refinements were carried out using the GSAS software [27], to determine lattice parameters and isotropic thermal displacement parameters (U_{iso}).

Sample	Ni	NiCoCr	HEA	T_H
T_m / K	1726	1725	1543	
T/ K	4.2	4.2	4.2	0.002
	64	64	57	0.037
	123	123	110	0.071
	182	182	162	0.106
	241		215	0.140
	291	291	268	0.174
			291	0.194

Table 1: Temperatures at which data were collected, melting temperature and homologous temperatures of the materials. Melting temperatures for Ni and NiCoCr samples calculated using the Thermocalc software using the TTNi5 Database. Melting temperature of NiCoCrMnFe taken from [2]

Processing of the total scattering data was carried out using the GudrunN software [28], and subsequent Fourier transforms to yield the PDFs were performed using the StoG routine (including the application of the Lorch function), distributed as part of the RMCProfile software package [29]. Subsequent fitting of the PDFs was carried out using small-box modelling methods in PDFgui [30], and individual peak fitting in Wavemetrics IgorPro. The term PDF is used to mean both $G(r)$ and $D(r)$ functions (as defined in equations 10 and 29 in Keen [31]) where $D(r) = 4\pi\rho_0 G(r)$ where ρ_0 is the average number density of the material.

The U_{iso} of the materials studied were obtained using four different methods to determine the reliability with which the lattice strain may be extracted. The labels used for these methods are as follows:

- **Bragg** - Fitting of the Bragg data using the GSAS software. The U_{iso} variable is a refineable parameter in the Rietveld fitting process, and then may be directly extracted from the output data files. It should be noted that this fitting will be highly susceptible to the absorption corrections used in the processing of the data. In the present study, absorption corrections were performed in the Mantid software. Fits were carried out both allowing the profile shapes to freely refine, and fixing the profile shapes to those of the high temperature sample. The two approaches were found to yield similar results, and the latter have been presented here.

- **PDF** - Fitting of the PDFs ($D(r)$) with the PDFGui software. This 'real-space' Rietveld method is capable of refining and outputting thermal parameters. The relationship between the parameters outputted from PDFGui and the U_{iso} is discussed in the Supplementary information.

- **PDFFIP** - Fitting of the PDFs ($D(r)$) with the PDFGui software - but fixing the instrumental parameters (Q_{damp} and Q_{broad}) to those that are recorded in the high temperature sample.

- **IPF** - Stands for 'Individual peak fitting'. The first n peaks in the PDF ($G(r)$) were fitted using an equation of the form:

$$G_{\mathrm{calc}}(r) = A\left[c_0 + \sum_{n=1}^{N} a_n \exp\left(- \frac{[r - (\frac{n}{2})^{\frac{1}{2}} r_0]^2}{2\sigma_{l,n}^2}\right)\right] \tag{21}$$

where c_0, a_n, r_0, A and $\sigma_{l,n}$ are refineable parameters. From this the widths of the first n peaks in the PDF were determined. The $(n/2)^{1/2}$ component arises due to the interatomic spacings in the *fcc* lattice, although not all values of n are possible ($n \neq 14, 30 \ldots$). The $\sigma_{l,n}$ parameters can then be used to estimate the thermal oscillation using eq. 19.

It is important to note (as discussed in [14]) that these measurements were made under the grey atom assumption - i.e. that the distribution of the elements in the material is random and hence that each atom can be treated as having the same average scattering power. Further, the first three measurements are all methods that measure offsite displacement u and so will yield a measure of the strain ε_u, whilst the IPF method is capable of yielding either ε_u or ε_l values [12] depending on the subsequent use of the fitted parameters $\sigma_{l,n}$ (see Supplementary information).

3.4. Calculation of U_{iso}

As mentioned previously, for the Bragg, PDF and PDFFIP methods, the U_{iso} values were outputted from the fitting software. For the IPF methodology, the first 28 peaks in the PDF were considered - chosen due to the absence of a peak at value $n = 30$ (and noting the absence peak at $n = 14$) providing a useful minima in the observed PDF. This yielded a measure of the peak widths $\sigma_{l,n}$ as a function of r. Commonly the peak widths in a PDF may be modelled by the equation:

$$\sigma_{l,n} = \sigma' \sqrt{1 - \frac{\delta_1}{r_n} - \frac{\delta_2}{r_n^2} + Q_{\mathrm{broad}}^2 r_n^2} \tag{22}$$

where r_n is the position of peak n, δ_1 and δ_2 are constants accounting for correlated motion, and Q_{broad} a broadening function resulting from the instrumental resolution. σ' is a constant for the material that describes the width caused by the thermal and static displacements only. It is therefore possible to fit the IPF widths with eq. 22 and so estimate σ'. (An example of such a fit, may be found in the supplementary information). Normally, only one of δ_1 or δ_2 is implemented, as they tend to refine strongly against one another. In the analysis of data in this study, δ_1 was set to zero and only δ_2 was allowed to refine, as it is believed that δ_2 better models low temperature correlated motion behaviour [32].

It should be noted that this is the same equation used to predict the peak widths in PDFGui. The difference with fitting by this method (compared with the PDF method) is that it allows arbitrary scaling of the areas of individual

peaks, and the simultaneous fitting of all the data sets. Therefore, it is possible to fit the data, with the same Q_{broad} for all samples at all temperatures (Q_{broad} is a function of the instrument on which the sample was measured, so should be independent of temperature). Similarly, δ_2 can be restricted for a given sample so that it is the same for all temperatures; or allowed to refine freely. Both of these methods were tried, with the data acquired in this study, but the two were found to yield similar values of strain, so the former is shown here (as it is more consistent with the fixed profiles used in GSAS and PDFFIP methods).

3.5. Separation of static, thermal and instrumental components

To assess the relative magnitude of the static strains in the system, three contributing terms to the observed offsite displacements and peak widths need to be isolated. In general if an isotropic offsite displacement U_{iso} is measured then:

$$U_{\mathrm{iso}} = U_S + U_T + U_I \tag{23}$$

where S denotes the static component, T the thermal, and I broadening from the instrumental components and processing (e.g. choice of Q_{max}). Combining eq. 23 and eq. 4:

$$U_{\mathrm{iso}} = \frac{3\hbar^2}{Mk{\theta_D}^2} T\Big(f(x) + \frac{x}{4}\Big) + U_S + U_I \tag{24}$$

As all measurements were carried out on the same instrument, and the data subjected to the same processing parameters, the instrumental term U_I should be constant across all the samples. Therefore, if the static and dynamic components of one of the materials can be found, the instrumental broadening can be determined. This can be done by using a pure element standard.

A pure element, such as nickel (measured in this experiment), should contain no associated static strains (assuming that strains caused by vacancies, mosacity and surface effects are negligible), i.e. $U_S = 0$. From equation 23 this means that there are only two components: U_I a constant at all temperatures, and U_T that varies as a function of temperature. By fitting the pure element data with eq. 24 and assuming $U_S = 0$, the instrumental broadening U_I can be calculated.

The data from other alloys measured on the same instrument and processed using the same parameters, can then be measured and the instrumental component removed, to yield U_S. M was taken as the average atomic mass of the species in the alloy. These were calculated from the NIST database using the compositions given previously, as $M_{\mathrm{Ni}} = 58.693$, $M_{\mathrm{NiCoCr}} = 57.048$ and $M_{\mathrm{HEA}} = 56.113$ amu.

4. Results

An exemplar Rietveld fit (for data from one of the instrument detector banks) carried out it the GSAS software is shown in Fig. 1. All of the fits

demonstrated that the materials were well described by a single *fcc* solution, with no indication of preferred orientation. There is a slight discrepancy in the intensity of the lowest Q peak, which is common for time of flight diffractometers. This is consistent for all the samples investigated, but may yield slight variations in the accuracy of the U_{iso} terms measured through the Bragg methodology discussed in section 3.3.

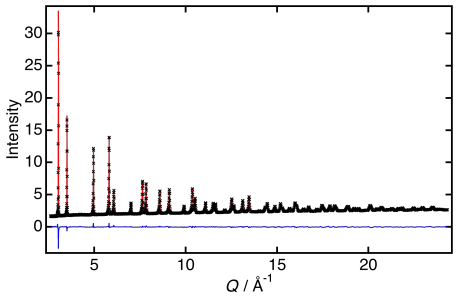

Figure 1: Example GSAS fit of Bank 4 ($2\theta \sim 90°$) data from the HEA sample measured at 4K with Rwp = 0.0175 (for all banks Rwp=0.0195). Black crosses indicate the data, red line - Rietveld fit, blue line - difference plot.

The resultant normalised PDFs are given in Figure 2. Figure 2(a) shows the variable temperature PDFs for the HEA sample. Figure 2(b) shows an expanded version of the first two PDF peaks from (a). A $Q_{\mathrm{max}} = 50\text{Å}^{-1}$ for the Fourier transform, carried out using the SToG routine (part of the RMCProfile software), and a Lorch function were applied (the choice of these parameters is discussed in the supplementary information).

The PDFs are all consistent with well defined crystalline materials. The peaks are broadest for the highest temperature (and narrowest at the lowest temperature), as expected for thermal broadening, arising as a result of increased thermal atomic displacements. A similar plot of the PDFs for the Ni and NiCoCr samples may be found in the supplementary information, and demonstrate similar features to that described for the HEA.

Figure 3(a) shows the low-r region of the normalised PDFs for the three samples recorded at 4K. It is apparent that there is a shift in the peaks of the three samples, corresponding to the different lattice parameters ($a_{\mathrm{HEA}} > a_{\mathrm{NiCoCr}} > a_{\mathrm{Ni}}$). Visually, there is no obvious difference between the widths of the PDF peaks. Figure 3(b) shows the same PDFs as Figure 3(a), but for the high-r region. If a lattice were to be highly-strained, it would be expected for the broadening in the PDFs at high-r to be much greater than for less strained materials, resulting in a featureless PDF (as is observed for amorphous materials). However, all the peaks in the PDF remain sharp at large distances, with comparable broadening (* denotes the peak from the same correlation shell in the PDF).

To assess further whether there is any strain broadening in these materials, the fitting methods outlined in Section 3.3 were employed to obtain U_{iso} values,

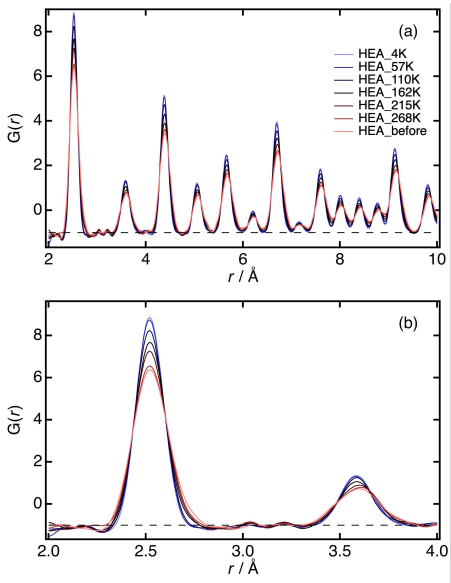

Figure 2: Plots of the normalised pair distribution functions. (a) Plots of the normalised $G(r)$s for the HEA sample from cold (blue) to hot (red) (b) magnified view of the data in (a) in the region 2.0 to 4.0 Å. The Ni and NiCoCr plots can be found in the supplementary information).

and the results shown in Fig. 4. To separate the static component from the thermal and instrumental, the calculated U values were further fitted with the equations outlined in section 3.5.

The data and fits for the three samples using the Bragg and PDF methodologies are shown in Fig. 4. The results from the PDFFIP method are similar to those from the PDF method, and are not shown here for clarity. However, for comparison these results can be found in the supplementary information. As can be seen at higher temperatures (above ∼100 K) the U_{iso} values increase approximately linearly, whilst at low temperature they tend to constant values. Importantly, the data are well described by the Debye equation (solid and dotted lines). In general, the U_{iso} values obtained using the Bragg method are lower than those from the fitting of the PDF with PDFGui. This in unsurprising given that the application of the Lorch function will result in an additional broadening of the PDF peaks, yielding a high observed U_{iso}, which will ultimately yield a higher U_{I} term.

By fitting the U_{iso} values with eq. 24, the U_S and θ_D values were obtained, and are tabulated in Table 2. This table also contains the $\bar{u}_S = \sqrt{U_S} = \sigma_{u,S}$ and the calculated value of the offsite strain $\varepsilon_{u,\mathrm{static}} = \frac{\sigma_{u,S}}{\bar{r}}$ [12].

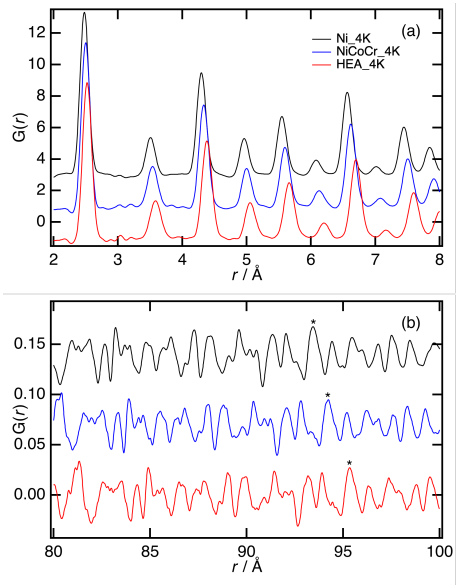

Figure 3: Plots of the normalised pair distribution functions. (a) Plot of the normalised $G(r)$s for the three samples, as measured at 4K: Ni - Black, NiCoCr - Blue, HEA - Red. (b) Plot of the normalised $G(r)$s for the three samples as measured at 4K, shown for the high-r region (colouring as for (a)). The PDFs have been offset vertically from one another for clarity. Asterisks (*) in (b) are to identify a peak in the PDF that corresponds to the same coordination shell in the material, to help guide the reader's eye.

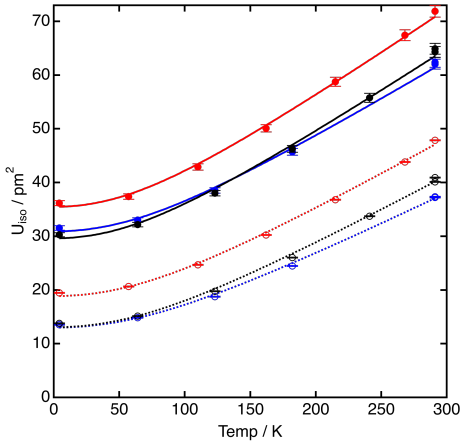

Figure 4: U_{iso} values and fits for the Rietveld refinements of the Bragg data (open circles and dotted line) and PDF values (filled circles and solid line). Black - Ni, Blue - NiCoCr, Red - CrMnCoFeNi. Fits done using the Debye equation for the three samples. The fitted parameters can be found in Table 2.

Table 2: Calculated values of static Debye-Waller factor U_{S}, root-mean squared offsite static displacement $\sigma_{u,S}$, Debye temperature θ_D, static strain offsite displacement $\varepsilon_{u,S}$, and bond length static strain $\varepsilon_{l,S}$ from different methods

Alloy		Ni	NiCoCr	CrMnFeCoNi
U_S / pm^2	Bragg	0	0.41 ± 0.12	5.16 ± 0.12
	PDF	0	1.75 ± 0.564	5.14 ± 0.59
	PDFFIP	0	2.50 ± 0.29	6.25 ± 0.32
	IPF	0	1.91 ± 0.08	4.84 ± 0.09
	IPF Peak1	0	-0.16 ± 0.18	1.98 ± 0.21
$\sigma_{u,S}$ / pm	Bragg	0	0.64 ± 0.09	2.27 ± 0.03
	PDF	0	1.32 ± 0.21	2.27 ± 0.13
	PDFFIP	0	1.58 ± 0.09	2.50 ± 0.06
	IPF	0	1.38 ± 0.03	2.20 ± 0.02
	IPF Peak1	0	-0.4 ± 0.23[1]	1.41 ± 0.07
θ_D / K	Bragg	429 ± 1	456 ± 1	430 ± 1
	PDF	390 ± 3	413 ± 4	390 ± 4
	PDFFIP	396 ± 2	424 ± 2	401 ± 2
	IPF	438 ± 1	454 ± 1	434 ± 1
	IPF Peak1	525 ± 2	565 ± 3	543 ± 3
$\varepsilon_{u,S} \times 100$	Bragg	0	0.51 ± 0.07	1.79 ± 0.02
	PDF	0	1.06 ± 0.17	1.79 ± 0.10
	PDFFIP	0	1.26 ± 0.07	1.97 ± 0.05
	IPF	0	1.10 ± 0.02	1.74 ± 0.02
$\varepsilon_{l,S}$	IPF Peak1	0	-0.16 ± 0.09	0.56 ± 0.03
δ_2 / Å^2	IPF	1.60 ± 0.02	1.99 ± 0.02	2.03 ± 0.03

5. Discussion

5.1. Comparison of the different methodologies

The methodologies for mathematically extracting the local lattice distortion described in Section 3.3 can be divided into two groups; those derived from average structural information (Bragg) and those derived from local structural information (PDF, PDFFIP, IPF). A comparison of this can be seen in Fig. 4 where the U_{iso} values from the Bragg methodology are presented, along with those from the PDF methodology. For both methodologies it is apparent that the U_{iso} values for the HEA are the highest for the three samples at a given temperature (or a given homologous temperature). This suggests that the magnitude of the local strain is indeed highest for the HEA out of the samples considered.

One notable difference between the Bragg and PDF methods can be seen in the results obtained from the Ni and NiCoCr samples. Specifically, the U_{iso}

values from the Bragg method are lower for the NiCoCr than the Ni sample for all temperatures considered. As the instrumental broadening effect on the two should be identical, and the thermal displacements are being taken into account, this would imply that the NiCoCr has a lower level of local strain than Ni. As an alloy, the NiCoCr would be expected to contain more local strain than the Ni, and therefore suggests that data processing uncertainties, such as the absorption correction, may be causing significant variations in the magnitude of the GSAS U_{iso} values measured. This demonstrates why values of local strain obtained from fitting the decay of the Bragg peaks with the Debye-Waller factor should be treated with caution.

In general, it is suggested that methods relating to a measurement from the local structure, are likely to provide a more accurate determination of the local lattice strain, and will be the primary focus for discussion going forward. Comparing the numerical results of these different methods (PDF, PDFFIP, IPF) shown in Table 2 many of the values are of a similar magnitude and within error (this will be discussed in more depth in the next section). Even for those not within error, the qualitative trends between these are the same (e.g. $\sigma_{u,S}$ increases from Ni to NiCoCr to CrMnFeCoNi for all methods).

The relative merits of these methods is probably therefore, better considered from a theoretical standpoint. Strictly speaking the instrument parameters should not change between the different measurements and therefore the PDFFIP method should prove more physically accurate than the PDF method. However, by reducing the available fitting parameters, the quality of the fit compared with the PDF method may be reduced. By fitting individual peaks with the IPF method, these may also account for any short range chemical variations (assuming a grey atom model) that are not accounted for when performing a PDFGui fit. Such a fit could more accurately model the variation in peak widths as a function of r and so provide a more accurate measure of the U_{iso} values.

Whichever method is chosen, it is important that it is clearly stated. Whilst for a qualitative comparison of several materials made in the same experiment any of these methods may suffice, for absolute quantification it is important to understand and clearly state the methodology used to derive such values. This is also important for the choice of processing parameters such as Q_{max} for the Fourier transform and the application of the Lorch function. A discussion of the choice of these parameters, and the effect on the resultant values, is included in the supplementary information.

5.2. Local lattice distortion of NiCoCr and CrMnFeCoNi

As already noted from Fig. 4, it appears that irrespective of the method, the U_{iso} values for the HEA are the highest for the three samples at a given temperature (or a given homologous temperature). Considering the other two materials, from the PDF results it appears that at higher temperatures (closer to room temperature) the Ni sample demonstrates a greater level of local displacement than the NiCoCr, whilst at low temperatures (where the thermal component is reduced) the local displacement NiCoCr is indeed higher, due to a greater magnitude of static offsite displacement.

Consider the measured displacements and strains shown in Table 2. The $\sigma_{u,S}$ for nickel, shown in Table 2, were set to zero by definition and serve as a baseline against which the other alloys may be compared. Recalling that $\sqrt{U_{\text{iso}}} = \sigma_{u,S}$, comparisons of $\sigma_{u,S}$ will be entirely equivalent to comparisons of U_{iso} and so the former will be discussed here.

Comparing the $\sigma_{u,S}$ values, shown in Table 2, it is apparent that both the NiCoCr and HEA exhibit some degree of static offsite displacement. Irrespective of the data processing methodology, the displacement is greater for the HEA than for the NiCoCr (this was also noted in Section 5.1 with regards to Fig. 4). In general, the values obtained from the three local structure data analysis methods (PDF, PDFFIP and IPF) are in good agreement with one another. It is apparent however, that the NiCoCr displacements measured from the Bragg data are somewhat lower than the comparative PDF measurements. As already noted, the lower U_{iso} values from the Bragg data of the NiCoCr are a source of concern and, indeed, the validity of this measurement has already been questioned given that is not a local structural probe.

From the $\sigma_{u,S}$ values it is possible to calculate an $\varepsilon_{u,S}$ using eq. 20, which can also be found in Table 2. For this conversion, the reference state of average atomic radius, $\bar{r}$, has been calculated using the lattice parameter from the Rietveld fit of the Bragg data at 4 K assuming a hard sphere model. It should be noted that as the temperature is increased the lattice expands due to thermal motion and therefore the apparent atomic radius will increase. Consequently, as the temperature increases the apparent value of the strain, $\varepsilon_{u,S}$ will decrease. Therefore, here the $\bar{r}$ values at 4 K have been used, as these are likely to give the most accurate values of the average atomic radius, excluding thermal effects, and will act as an upper bound of the possible values of the strain that may be calculated.

These values suggest that both alloys contain a level of static strain, with the HEA having a higher value than the NiCoCr. As discussed in [10], one metric for the comparison of lattice strains is the δ-parameter, which is of a similar form to $\varepsilon_{u,S}$. Often in the HEA literature a limit of $\delta = 0.066$ is given for the stability of the HEAs, which is numerically similar to the 15% atomic size difference guideline suggested by Hume-Rothery [33]. Therefore, whilst both alloys contain some level of strain, neither appears to demonstrate particularly high levels of strain compared with this stability limit, and consequently cannot be considered highly-distorted by this metric.

Figure 5 shows a plot of the relative contributions ($\sigma_{u,S}$, $\sigma_{u,T}$ and $\sigma_{u,I}$) to the measured U_{iso} values for the PDF methodology. By definition, the instrumental contribution (solid grey bars) is constant for all materials and temperatures. It should be noted again that the magnitude of the static displacements (black bars) for the Ni is zero. It is apparent that the HEA contains the largest level of static displacement (black bars). However, even at low temperatures, the magnitude of the static displacements is smaller than the comparative thermal component. No statement or quantitative limit exists in the literature that defines the magnitude of strain within a material that may be considered 'highly-strained'. A possible metric could be the ratio of thermal to static strains.

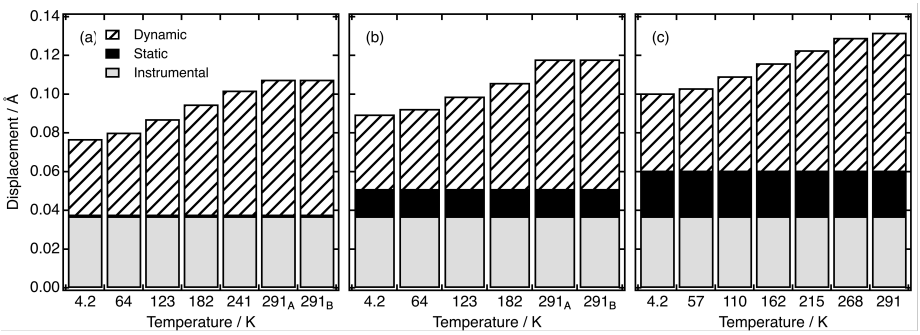

Figure 5: Relative contributions to the observed offsite displacement as a function of temperature for (a) Ni, (b) NiCoCr (c) HEA. ☐ - indicates contribution from instrumental broadening; ■ - the static component caused by local lattice strain; ▨ - the dynamic component resulting from thermal oscillations. Calculated from the PDF methodology data. The repeated 291K measurements on (a) and (b) represent measurements taken at room temperature from the sample before (291_B) and after (291_A) cooling

However, it is noted that by this metric, all of the ratios measured in this study would be less than unity. It is, therefore, not clear whether a ratio of greater than unity is a suitable metric to classify a material as highly strained. Although, it may be possible that ratios exceeding unity occur in other HEA systems containing species with greater atomic size differences.

5.3. Width of the first PDF peak, correlated motion and interatomic interaction strength

The final data analysis method, IPF Peak 1, considers only the width of the first peak in the PDF (obtained by peak fitting). In this case the peak width of the NiCoCr is narrower than that of the Ni and the HEA. However, the U_{iso} value measured from the higher-r peaks is consistent with the strain in the NiCoCr being higher than the strain in the Ni. This difference is attributable to the effect of correlated motion in the system. In a classical spring bonding model of a system, the motion of an atom will result in the correlated motion of bonded atoms. Consequently, peaks at low-r will be narrower than those at higher-r, where distant neighbouring atoms will move independently.

This suggests that the NiCoCr contains a greater level of correlated motion compared with the Ni sample. This results in an additional narrowing of the peak compared with the Ni, and this leads to an apparent $U_S = \sigma^2_{u,S} < 0$ [1] . This higher level of correlated motion is also reflected in the calculated values of δ_2 for the three materials shown in Table 2, which are higher for the NiCoCr and HEA than for the nickel. As $\sigma^2_{u,S} < 0$, this results in a $\varepsilon_{u,S} < 0$ for the NiCoCr for the IPF method. Additionally, in a system with no correlated

[1] As $\sigma^2_{u,S} < 0$, here we present $\sigma_{u,S} = -\sqrt{-\sigma^2_{u,S}}$

motion $\varepsilon_{u,S} = \sqrt{2}\varepsilon_{l,S}$, so a theoretical $\varepsilon_{l,S}$ for the HEA using the IPF method can be calculated from the $\varepsilon_{u,S}$ value as $\varepsilon_{\text{theoretical},l,S} = 1.23$. Comparing this to the experimental $\varepsilon_{l,S} = 0.56$ value demonstrates the additional contribution from the correlated motion effect. This shows the importance of considering both the $\varepsilon_{u,S}$ and $\varepsilon_{l,S}$ to fully understand what is taking place in the system.

Comparing the Debye temperatures, it is apparent that there is a wide spread in the values obtained. However, in most cases (data from the IPF Peak1 method being the exception) $\theta_{D,\text{Ni}} \approx \theta_{D,\text{HEA}} < \theta_{D,\text{NiCoCr}}$. Killean [24] suggested that:

$$\theta_D = \frac{2\hbar}{k}\left[\frac{2\phi^{II}(0)}{M}\right]^{\frac{1}{2}} \tag{25}$$

where M the atomic mass, $\phi^{II}(0)$ is the second derivative of the harmonic potential between the atoms, and is therefore a measure of the force constant and stiffness of the interatomic potential between the atoms. If the system were modelled by hard spheres connected by springs, this would suggest that the NiCoCr has the greatest force constant. Such an increase would also result in a higher degree of correlated motion, as observed in the $\varepsilon_{l,S}$. Considering the IPF Peak1 method θ_D values, this may further explain why the HEA has a higher θ_D value as this measurement more accurately captures the correlated motion effects, compared with the values obtained by other methods.

It should be noted that even in the cases where $\theta_{D,\text{Ni}} \approx \theta_{D,\text{HEA}}$ this suggests a higher degree of correlated motion in the HEA sample compared with the Ni as $M_{\text{Ni}} < M_{\text{HEA}}$.

Such considerations of the first peak in isolation are important - particularly in comparison between measurements made using different techniques. EXAFS and NMR can be useful probes of local environment, but can be limited in the number of correlation shells they are capable of probing. It is important, therefore, when considering values of local lattice strain calculated from these comparative techniques to consider the effect that correlated motion and the strength of interatomic interactions may have on the observed values.

6. Conclusions

A method of determining local lattice strains in alloys using total scattering measurements toward absolute zero has been presented. The method was used to assess the level of local lattice strain in the high-entropy alloy CrMnFeCoNi, from neutron total scattering data acquired over a range of temperatures, along with samples of Ni and Ni-37.5Co-37.5Cr-25 at.%. A number of different methodologies were used to calculate PDF peak widths and U_{iso} values for the materials at different temperatures. By fitting with an equation modelling the variation of Debye-Waller factors with temperature, it was possible to separate thermal components from the system. Using the Ni as a reference static strain free material, it was possible to estimate the instrumental contribution to the peak widths and assess the local lattice strains in the NiCoCr and HEA samples. Both $\varepsilon_{u,S}$ and $\varepsilon_{l,S}$ values were calculated.

From the $\varepsilon_{u,S}$ values it was apparent that both the NiCoCr and HEA contain static strains, with the level of static strain being greater in the HEA than the NiCoCr. However, both strains are considerably smaller than the indicator $\delta = 0.066$, which is widely considered the upper bound for strain that can be tolerated in a solid solution phase. Additionally, when considering the relative magnitude of the displacements, it is apparent that even at low temperatures the thermal offsite displacement is considerably larger than the static offsite displacement. Consequently, neither approach presents strong evidence that the lattices can be considered highly distorted.

Comparing the $\varepsilon_{l,S}$ values it is apparent that the NiCoCr and HEA both contain higher levels of correlated motion than the pure Ni sample. This is confirmed by the Debye temperatures, which imply a strongly increased bond stiffness in the NiCoCr sample and a possible increase in the HEA sample. Further exploration of the material using neutron spectroscopy may assist in elucidating the lattice dynamics of these materials. This also highlights the necessity for calculation of both $\varepsilon_{u,S}$ and $\varepsilon_{l,S}$ to fully describe the local environments of these materials.

Data access statement

The original research data are available at DOI: 10.5286/ISIS.E.RB1620375.The analysed data are available at : https://orda.shef.ac.uk.

Rights Retention

This work was funded by UKRI grant EP/ M005607/1. For the purpose of open access, the author has applied a Creative Commons Attribution (CC BY) licence to any Author Accepted Manuscript version arising.

Acknowledgements

Neutron beam time was provided by the ISIS Pulsed Neutron and Muon Source through experiment number: RB1620375. This work was supported by the STFC ISIS Facility and the Rolls-Royce /EPSRC Strategic Partnership under EP/ M005607/1. Dr Lewis Owen would like to thank Gonville and Caius College and the Royal Academy of Engineering (RAEng) for their ongoing support during his research fellowships.

References

[1] M. Tsai, J. Yeh, High-entropy alloys: A critical review, Materials Research Letters 2 (2014) 107–123.

[2] E. Pickering, N. Jones, High entropy alloys: A critical assessment of their founding principles and future prospects, International materials reviews 61 (3) (2016) 183–202.

[3] D. Miracle, O. Senkov, A critical review of high entropy alloys and related concepts, Acta Materialia 122 (2017) 448–511. doi:https://doi.org/10.1016/j.actamat.2016.08.081.
URL https://www.sciencedirect.com/science/article/pii/S1359645416306759

[4] E. P. George, D. Raabe, R. O. Ritchie, High-entropy alloys, Nature Reviews Materials 4 (8) (2019) 515–534. doi:10.1038/s41578-019-0121-4.
URL https://doi.org/10.1038/s41578-019-0121-4

[5] E. George, W. Curtin, C. Tasan, High entropy alloys: A focused review of mechanical properties and deformation mechanisms, Acta Materialia 188 (2020) 435–474. doi:https://doi.org/10.1016/j.actamat.2019.12.015.
URL https://www.sciencedirect.com/science/article/pii/S1359645419308444

[6] J. Yeh, Recent progress in high-entropy alloys, Annales de chimie - Science des Materiaux 31 (2006) 633–648.

[7] J.-W. Yeh, S. Lin, T. Chin, J. Gan, S. Chen, Formation of simple crystal structures in Cu-Co-Ni-Cr-Al-Fe-Ti-V alloys with multiprincipal metallic elements, Metallurgical and Materials Transactions A 35 (2004) 2533–2536.

[8] B. Murty, J. Yeh, S. Ranganathan, High-entropy alloys, Butterworth-Heinemann, 2014.

[9] N. G. Jones, L. R. Owen, Lattice distortion in high-entropy alloys, in: F. G. Caballero (Ed.), Encyclopedia of Materials: Metals and Alloys, Elsevier, Oxford, 2022, pp. 393–401. doi:https://doi.org/10.1016/B978-0-12-803581-8.12124-1.
URL https://www.sciencedirect.com/science/article/pii/B9780128035818121241

[10] L. Owen, N. Jones, Lattice distortions in high-entropy alloys, Journal of Materials Research 33 (19) (2018) 2954–2969.

[11] L. Owen, E. Pickering, H. Playford, H. Stone, M. Tucker, N. Jones, An assessment of the lattice strain in the crmnfeconi high-entropy alloy, Acta Materialia 122 (2017) 11–18.

[12] L. Owen, N. Jones, Quantifying local lattice distortions in alloys, Scripta Materialia 187 (2020) 428–433.

[13] P. Withers, H. Bhadeshia, Residual stress. part 1 – measurement techniques, Materials Science and Technology 17 (4) (2001) 355–365. arXiv:https://doi.org/10.1179/026708301101509980, doi:10.1179/026708301101509980.
URL https://doi.org/10.1179/026708301101509980

[14] L. Owen, H. Stone, H. Playford, The assessment of local lattice strains in alloys using total scattering, Acta Materialia 170 (2019) 38–49.

[15] H. S. Oh, D. Ma, G. P. Leyson, B. Grabowski, E. S. Park, F. Körmann, D. Raabe, Lattice distortions in the feconicrmn high entropy alloy studied by theory and experiment, Entropy 18 (9). doi:10.3390/e18090321.
URL https://www.mdpi.com/1099-4300/18/9/321

[16] L. Lilensten, K. Provost, L. Perrière, E. Fonda, J.-P. Couzinié, F. Amann, M. Radtke, G. Dirras, I. Guillot, Experimental investigation of the local environment and lattice distortion in refractory medium entropy alloys, Scripta Materialia 211 (2022) 114532. doi:https://doi.org/10.1016/j.scriptamat.2022.114532.
URL https://www.sciencedirect.com/science/article/pii/S1359646222000331

[17] Y. Zuo, S. Maiti, W. Steurer, R. Spolenak, Size-dependant plasticity in an $Nb_{25}Mo_{25}Ta_{25}W_{25}$ refractory high-entropy alloy, Acta Materialia 65 (2014) 85–97.

[18] C. Lee, G. Song, M. C. Gao, R. Feng, P. Chen, J. Brechtl, Y. Chen, K. An, W. Guo, J. D. Poplawsky, S. Li, A. Samaei, W. Chen, A. Hu, H. Choo, P. K. Liaw, Lattice distortion in a strong and ductile refractory high-entropy alloy, Acta Materialia 160 (2018) 158–172. doi:https://doi.org/10.1016/j.actamat.2018.08.053.
URL https://www.sciencedirect.com/science/article/pii/S1359645418306906

[19] S. Mu, S. Wimmer, S. Mankovsky, H. Ebert, G. Stocks, Influence of local lattice distortions on electrical transport of refractory high entropy alloys, Scripta Materialia 170 (2019) 189–194. doi:https://doi.org/10.1016/j.scriptamat.2019.05.032.
URL https://www.sciencedirect.com/science/article/pii/S1359646219303008

[20] N. L. Okamoto, K. Yuge, K. Tanaka, H. Inui, E. P. George, Atomic displacement in the CrMnFeCoNi high-entropy alloy – a scaling factor to predict solid solution strengthening, AIP Advances 6 (12) (2016) 125008. arXiv:https://doi.org/10.1063/1.4971371, doi:10.1063/1.4971371.
URL https://doi.org/10.1063/1.4971371

[21] Y.-Y. Tan, Z.-J. Chen, M.-Y. Su, G. Ding, M.-Q. Jiang, Z.-C. Xie, Y. Gong, T. Wu, Z.-H. Wu, H.-Y. Wang, L.-H. Dai, Lattice distortion and magnetic property of high entropy alloys at low temperatures, Journal of Materials Science and Technology 104 (2022) 236–243. doi:https://doi.org/10.1016/j.jmst.2021.07.019.
URL https://www.sciencedirect.com/science/article/pii/S1005030221007325

[22] P. Debye, Interferenz von Röntgenstahlen und wärmebewegung, Annalen der Physik 348 (1) (1913) 49–92.

[23] I. Waller, Zur frage der einwirkung der wärmebewegung auf die intergerenz von röntgenstrahlen, Zeitschrift fur Physik 17 (1923) 398–408.

[24] R. Killean, An investigation of the Debye-Waller factor and Debye temperature of aluminium using nearest neighbour central force pair interactions, Journal of Physics F: Metal Physics 4 (11) (1974) 1908.

[25] O. Arnold, J. Bilheux, J. Borreguero, A. Buts, S. Campbell, L. Chapon, M. Doucet, N. Draper, R. F. Leal, M. Gigg, V. Lynch, A. Markvardsen, D. Mikkelson, R. Mikkelson, R. Miller, K. Palmen, P. Parker, G. Passos, T. Perring, P. Peterson, S. Ren, M. Reuter, A. Savici, J. Taylor, R. Taylor, R. Tolchenov, W. Zhou, J. Zikovsky, Mantid—data analysis and visualization package for neutron scattering and μ SR experiments, Nuclear Instruments and Methods in Physics Research Section A: Accelerators, Spectrometers, Detectors and Associated Equipment 764 (2014) 156 – 166.

[26] F. Akeroyd, S. Ansell, S. Antony, O. Arnold, A. Bekasovs, J. Bilheux, J. Borreguero, K. Brown, A. Buts, S. Campbell, D. Champion, L. Chapon, M. Clarke, S. Cottrell, R. Dalgliesh, D. Dillow, M. Doucet, N. Draper, R. Fowler, M. A. Gigg, G. Granroth, M. Hagen, W. Heller, A. Hillier, S. Howells, S. Jackson, D. Kachere, M. Koennecke, C. Le Bourlot, R. Leal, V. Lynch, P. Manuel, A. Markvardsen, R. McGreevy, D. Mikkelson, R. Mikkelson, R. Miller, S. Nagella, T. Nielsen, K. Palmen, P. G. Parker, M. Pascal, G. Passos, T. Perring, P. F. Peterson, F. Pratt, T. Proffen, P. Radaelli, J. Rainey, S. Ren, M. Reuter, L. Sastry, A. Savici, J. Taylor, R. J. Taylor, M. Thomas, R. Tolchenov, R. Whitley, M. Whitty, S. Williams, W. Zhou, J. Zikovsky, Mantid: Manipulation and analysis toolkit for instrument data., Mantid Project.

[27] A. C. Larson, R. B. V. Dreele, General structural analysis system (GSAS), Los Alamos National Laboratory Report LAUR (2000) 86–748.

[28] A. K. Soper, GudrunN and GudrunX : programs for correcting raw neutron and X-ray diffraction data to differential scattering cross section, Rutherford Appleton Laboratory Technical report RAL-TR-2001-013.

[29] M. G. Tucker, D. A. Keen, M. T. Dove, A. L. Goodwin, Q. Hui, RMCProfile: reverse Monte Carlo for polycrystalline materials, Journal of Physics: Condensed Matter 19 (33).

[30] C. L. Farrow, P. Juhas, J. W. Lui, D. Bryndin, E. S. Bozin, J. Bloch, T. Proffen, S. Billinge, PDFfit2 and PDFGui: computer programs for studying nanostructure in crystals., Journal of Physics: Condensed Matter 19 (33).

[31] D. A. Keen, A comparison of various commonly used correlation functions for describing total scattering, Journal of Applied Crystallography 34 (2001) 172–177.

[32] I. Jeong, R. Heffner, M. Graf, S. Billinge, Lattice dynamics and correlated atomic motion from the atomic pair distribution function, Physical Review B 67.

[33] W. Hume-Rothery, G. V. Raynor, The Structure of Metals and Alloys, Institute of Metals, 1954.